Real-time Free-moving Active Coded Mask 3D Gamma-Ray Imaging

Daniel Hellfeld, Paul Barton, Donald Gunter, Andrew Haefner, Lucian Mihailescu, and Kai Vetter

***Abstract*—The ability to localize and map the distribution of gamma-ray emitting radionuclides in 3D has applications ranging from medical imaging to nuclear security. In the case of radiological source search and nuclear contamination remediation, the deployment of freely moving detection systems such as hand-held instruments or ground/aerial-based vehicles are critical in overcoming the inverse square law and complex shielding scenarios. Using contextual sensors, these systems can simultaneously generate 3D maps of the surrounding environment and track the position and orientation of the gamma-ray sensitive detectors in that environment. The fusion of contextual scene data and gamma-ray detector data to facilitate real-time 3D gamma-ray image reconstruction has been demonstrated with mobile HPGe and CdZnTe-based Compton cameras for gamma-ray energies ranging from a few hundred keV to several MeV. Here we apply this approach for lower energy (50−400 keV) gamma-rays, using a hand-held CdZnTe-based omnidirectional imaging system and an active coded mask imaging modality. We present our approach to real-time reconstruction using a scene data constrained GPU-accelerated list-mode MLEM algorithm and show results from several measurements in the lab and in the field.**

***Index Terms*—3D gamma-ray imaging, spherical active coded mask, real-time imaging, scene data fusion**

I. Introduction

THE detection, characterization, localization and mapping of gamma-ray source distributions are critical in fields such as gamma-ray astronomy, medical imaging and nuclear security. In the case of nuclear security, free-moving systems are needed to efficiently find sources in potentially cluttered environments or complex shielding scenarios as well as to quickly map radiation fields across large areas. The distinction of a free-moving system is made here to discriminate between portable systems that are designed to acquire data in several static positions and mobile systems designed to acquire gamma-ray data while the system is in continuous motion with no constraints on position or orientation.

In radiological source search, hand-held free-moving systems are important in overcoming the inverse square law to get much closer to weaker sources or to view suspected source locations from various perspectives in order to circumvent potential shielding (e.g., finding narrow streaming paths) [1], [2], [3], [4]. In nuclear contamination remediation and consequence management, unmanned ground-based or aerial-based systems facilitate quick wide-area mapping of gamma-ray source distributions while limiting dose to human operators [5], [6], [7], [8], [9]. These maps can be used as a guide for further remediation, to ensure the area is no longer contaminated, or for contamination avoidance planning.

Traditionally, such mobile systems consist of non-imaging detectors and produce proximity images or maps, using only the gamma-ray flux modulation with distance as a means for localization or source distribution estimation [9], [10]. Imaging capabilities can significantly enhance the localization of sources and the mapping of complex distributions, though the current state-of-the-art commercially available imagers [11], [12] are designed for static data acquisition and produce 2D images. While sometimes combined with a visual camera overlay for context, 2D images in many cases can result in ambiguity as to the true location of the source relative to the 3D scene (e.g., in or behind a box, in front or behind a wall). Furthermore, the static standoff measurements may require long dwell times (tens of min) to image weak or shielded sources. In other cases, 2D gamma-ray images are projected onto laser-based 3D models of the surrounding environment [13], though this approach still suffers from the same ambiguity problem when only one static gamma-ray measurement is performed. The introduction of unrestricted motion to these imaging systems can improve detection sensitivity while facilitating 3D gamma-ray imaging.

The system position and orientation (i.e., pose) must be known at every measurement in order to image in 3D. In contrast to medical imaging, in which the detector system has a fixed and known geometry relative to a stationary image space, free-moving systems require auxiliary sensors and tracking algorithms for accurate pose estimation. Mihailescu et al. [14] demonstrated 3D imaging with a mobile system by first acquiring data from multiple static locations around a source and manually determining the system pose at each measurement using a laser rangefinder. More recent work has developed the use of simultaneous localization and mapping (SLAM) [15], [16] for real-time pose tracking of continuously moving mobile systems. This was first demonstrated with RGB-D Microsoft Kinect cameras and RGB-D SLAM [17] on a free-moving cart-based double-sided-strip HPGe detector [18] and a hand-held dual-plane CdZnTe detector array [19]. The active infrared depth sensors on the Kinect have a range of 4−6 m and are limited to indoors mapping scenarios.

Manuscript received September 4, 2019. This material is based on work supported by the Department of Energy National Nuclear Security Administration through the Nuclear Science and Security Consortium under Award No. DE-NA0003180 and by the Defense Threat Reduction Agency under Contract Number DTRA10027-19346. This support does not constitute an expressed or implied endorsement on the part of the United States Government.

D. Hellfeld is with the Nuclear Engineering Department at the University of California (UC), Berkeley, Berkeley, CA 94720 USA (email: dhellfeld@berkeley.edu).

P. Barton, D. Gunter and L. Mihailescu are with the Applied Nuclear Physics program at Lawrence Berkeley National Laboratory, Berkeley, CA 94720 USA.

A. Haefner is now with Openwater, San Francisco, CA 94111 USA.

K. Vetter is with the Nuclear Engineering Department at UC Berkeley and the Applied Nuclear Physics program at Lawrence Berkeley National Laboratory, Berkeley, CA 94720 USA.

Other work has demonstrated the use of light detection and ranging (LiDAR) sensors for indoor, outdoor, and wide-area (10−100 m) SLAM on a variety of manned and unmanned platforms [20], [21].

In addition to pose estimation, SLAM generates a 3D model of the environment around the detector. The 3D scene model can be used to provide context to the 3D gamma-ray image and to constrain the image reconstruction, increasing image accuracy, decreasing noise, and improving the computational efficiency of the reconstruction. This approach is referred to as scene data fusion (SDF) [18]. The contextual tracking and mapping as well as gamma-ray imaging can be performed in real-time, providing a 3D scene and gamma-ray model to the user during a measurement, allowing for course correction and decreasing the time to detect and image suspected sources.

Previous work has focused on the Compton imaging modality for gamma-ray energies from several hundred keV to a few MeV. Here we extend these concepts to the active coded mask modality for lower gamma-ray energies (tens of keV to a few hundred keV) of significant interest to nuclear security, safeguards and nonproliferation. We present our approach to real-time 3D imaging using the maximum likelihood expectation maximization (MLEM) reconstruction algorithm [22] in the list-mode formalism [23] with graphics processing unit (GPU) acceleration. Several reconstruction scenarios are shown, both in the lab and in the field. The measurements in this work are limited to unshielded point-sources, with activities ranging from μCi (37 kBq) to mCi (37 MBq) and gamma-ray energies from 59 to 356 keV. The Portable Radiation Imaging Spectroscopy and Mapping (PRISM) detector system, described below, is used here as the platform for development and demonstration.

This paper is organized as follows: the PRISM detector system is described in Sec. II, the 3D coded mask imaging and SDF approach is presented in Sec. III, the real-time imaging results are shown in Sec. IV, and conclusions in Sec. V.

II. PRISM

The PRISM system is a free-moving hand-held spherical active coded array of many 1 cm^3 coplanar-grid (CPG) [24], [25] CdZnTe (CZT) detector modules, designed for omnidirectional dual-mode (coded mask and Compton) gamma-ray imaging (see Fig. 1). The first prototype design and demonstration of 4π active coded mask imaging was previously described in [26]. In this work, we utilize the next iteration of the prototype system, hereby referred to as PRISM-v1. A brief overview of the system is provided here, but a more detailed description and characterization will be presented in future work.

The $\varnothing$14 cm spherical array was designed with a total of 192 available detector slots. Currently, 100 detectors are loaded in the sphere, in an optimal configuration for coded mask imaging. The optimization of the number and configuration of detectors was addressed in our previous work [26]. Each CPG-CZT detector crystal is connected to a dedicated application specific integrated circuit (ASIC) board to read-out, process (i.e., collecting and non-collecting anode grid differencing with relative gain), shape and amplify both the anode grid and cathode signal waveforms [27]. The modules (crystal and ASIC) are packaged in Lexan casings that snap into the interior of the spherical enclosure. The crystals are oriented such that the cathodes face in towards the center of the sphere. A flexible circuit connects the individual ASIC boards to 12 analog-to-digital converter (ADC) cards (384 channels) on the signal acquisition motherboard. A total of 384 channels are available for processing the anode and cathode signals of all 192 detector slots, allowing for the number and configuration of the detector modules to change without modification to the electronics pipeline. The digitized signals are processed with a field programmable gate array (FPGA) on a digital signal processing board based on the CAPTAN architecture [28]. The processed signals are then routed to a single-board computer (Intel NUC7i7BNH [29]) via ethernet for further data processing, analysis and image reconstruction.

The auxiliary sensor package includes an optical camera (FLIR flea3 camera [30] with Kowa 3.5 mm/F1.4 lens [31]), LiDAR (Velodyne Puck Lite [32]) and inertial measurement unit (IMU) (VectorNav VN-200 [33]) for real-time contextual mapping and tracking. Contextual data processing and SLAM (via the Google Cartographer package [34]) are also performed on the onboard computer. A wireless tablet is used for real-

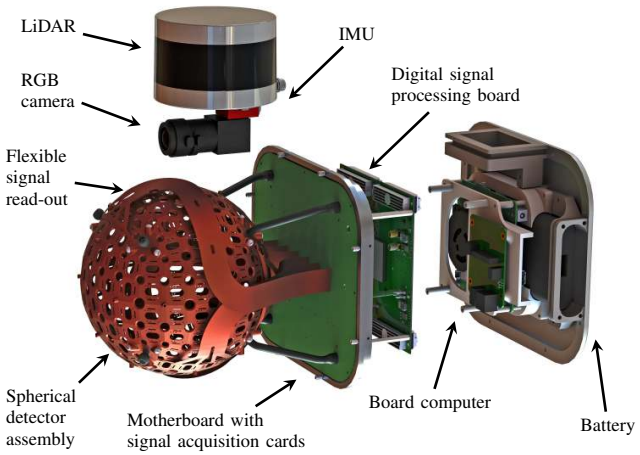

Fig. 1. (Color online) (Top) PRISM-v1 prototype system with accompanying wireless tablet for remote control and visualization. (Bottom) Annotated diagram of PRISM-v1 components and internal design. The 1 cm^3 CZT detector modules (packaged with individual read-out ASIC boards) snap into the interior of the spherical enclosure with the CPG anodes facing outwards.

time remote control and visualization, connected to the system via WiFi. A single 98 Wh Li battery powers the entire system for $\sim$1 hr, though the battery life may fluctuate depending on the demand placed on the computer (e.g., from image reconstruction and SLAM). The system can be powered on and begin acquiring data in $<$ 30 s. With the battery attached, the system weight is approximately 6.35 kg.

Each CPG module read-out facilitates the event-by-event determination of depth-of-interaction (DOI) along the anode-cathode axis. The increase in information density of each event and the higher frequency features in the low-energy response will improve the angular (and spatial) resolution of the active coded mask imaging modality. The depth sensitivity also improves Compton imaging by reducing the lever arm uncertainty. A thorough characterization of the DOI response of PRISM-v1 and the implementation of DOI into the real-time 3D imaging approach will be the subject of future work. Only the anode signals were utilized for event reconstruction in the work presented here.

III. Methods

A. Active Coded Mask Imaging

The traditional coded aperture approach [35] utilizes a passive high-Z (e.g., Pb, W) mask in front of a position-sensitive gamma-ray detector. The mask is designed to uniquely modulate the incident gamma-ray flux based on the source direction (i.e., the spatial pattern of events in the detector uniquely determines the direction of the source). The reconstruction of the estimated source distribution is typically limited to a region-of-interest (ROI) in energy, using only full-energy absorption (i.e., photopeak) events. The effectiveness of the coded mask decreases with increasing energy as the attenuation of photons weakens and the detection pattern blurs.

The passive mask approach presents several problems for imaging systems of relevance for radiological source search and distributed source mapping. First, the reconstruction relies on gamma-ray events being discarded. This is not ideal in count-starved scenarios such as weak or shielded source search, where statistics are important to solve the detection problem. Second, the weight of the mask material can result in cumbersome detectors, limiting the overall mobility of free-moving systems. Third, the traditional planar construction of these types of imagers suffers from a limited coded field-of-view (FOV). Finally, the characteristic fluorescence photons (58$-$85 keV) from high-Z masks can obstruct low-energy reconstruction such as the 59 and 81 keV lines from ^{241}Am and ^{133}Ba, respectively [36].

The replacement of passive mask materials with active (detector) elements has been explored to increase sensitivity, decrease weight, improve the coded FOV, and enable Compton imaging [37], [38]. The PRISM system was the first to introduce and experimentally demonstrate a spherical active coded mask design for omnidirectional coded mask and Compton imaging. The coded mask imaging modality is used in the energy range of 50$-$400 keV in PRISM-v1. Above this range, the gamma-ray mean free path is larger than the average path length through a 1 cm^3 cube and the Compton scattering cross-section is $\sim$2 times larger than photoelectric absorption. Below this range, the data are dominated by background, down-scatter and low-energy electronics noise.

B. List-mode MLEM

Given a set of I measurements, $\boldsymbol{x}^{[I\times 1]} = [x_1, x_2, \ldots, x_I]^T$, we wish to solve for the distribution of J source intensities in a voxelized spatial domain, $\boldsymbol{\lambda}^{[J\times 1]} = [\lambda_1, \lambda_2, \ldots, \lambda_J]^T$, from which the measured data originated. The source intensities are related to the measurement space by

$$\bar{\boldsymbol{x}} = \boldsymbol{C}\cdot\boldsymbol{\lambda}\,, \tag{1}$$

where $\bar{\boldsymbol{x}}$ are the mean-rates and $\boldsymbol{C}^{[I\times J]}$ is the system matrix, which describes the geometric and detector efficiency of the I measurements relative to the J image voxels, given by

$$C_{ij} \approx \eta_{ij}\xi_{ij}t_i|\vec{r}_i - \vec{r}_j|^{-2}\,, \tag{2}$$

where η_{ij} is the angular response of measurement i to image voxel j, t_i is the integration time of measurement i, $\vec{r}_i$ and $\vec{r}_j$ are the global position coordinates associated with measurement i and image voxel j, respectively, and ξ_{ij} is the transmission probability of a gamma-ray between $\vec{r}_i$ and $\vec{r}_j$. The angular response is determined either through measurement or simulation. In this work, the angular response of PRISM-v1 was generated in the far-field limit using Monte Carlo simulations in Geant4 [39]. All measurements in this work were performed with source standoffs appropriate for the far-field approximation ($>$ 75 cm). The transmission probability matrix was assumed to be unity everywhere due to unknown voxel material composition and the additional computational burden of pose-to-voxel ray-casting.

Due to the individual counting of discrete events, gamma-ray measurements follow Poisson statistics. The negative log of the Poisson likelihood of measuring $\boldsymbol{x}$ given $\boldsymbol{\lambda}$ is

$$\ell(\boldsymbol{x}|\boldsymbol{\lambda}) = [\boldsymbol{C}\cdot\boldsymbol{\lambda} - \boldsymbol{x}\odot\log(\boldsymbol{C}\cdot\boldsymbol{\lambda}) + \log[\Gamma(\boldsymbol{x}+1)]]^T\cdot\mathbf{1}\,, \tag{3}$$

where $\odot$ denotes element-wise multiplication and $\Gamma(\cdot)$ is the gamma function. MLEM is an iterative algorithm that solves for an estimate of the source intensity distribution $\hat{\boldsymbol{\lambda}}$ that maximizes the likelihood, or minimizes $\ell(\boldsymbol{x}|\boldsymbol{\lambda})$. The computational complexity of each MLEM iteration is $\mathcal{O}(IJ)$. In a "bin-mode" formulation of MLEM [22], the dimension I is of size $P\times D$ where P is the number of poses and D is the number of detectors. A typical free-moving measurement scenario can contain 10^3 to 10^4 poses, therefore I can easily be on the order of 10^5 to 10^6 when using the PRISM-v1 system with 100 detectors. In most cases, the number of measured gamma-ray counts N in a particular ROI is significantly smaller than $P\times D$. Therefore a "list-mode" formulation of MLEM [23], in which the dimension I is of size N, is more appropriate for this type of imaging problem.

The list-mode data $\boldsymbol{x}^{[N\times 1]}$ consists of N events, where each event x_n represents a single measured interaction in detector $d\in[1,D]$ at pose $p\in[1,P]$ with energy deposition E in some ROI (e.g., 122 ± 10 keV). The $\{n,j\}$ element of the system matrix $\boldsymbol{C}^{[N\times J]}$ represents the probability of a gamma-ray emitted from voxel j producing event x_n. The list-mode MLEM update equation (at iteration $q+1$) is given by

$$\hat{\boldsymbol{\lambda}}^{q+1} = (\hat{\boldsymbol{\lambda}}^{q}\oslash\boldsymbol{\varsigma})\odot\boldsymbol{C}^T\cdot[\mathbf{1}\oslash(\boldsymbol{C}\cdot\hat{\boldsymbol{\lambda}}^{q})]\,, \tag{4}$$

where $\oslash$ denotes element-wise division. The sensitivity $\boldsymbol{\varsigma}^{[J\times 1]} = \widetilde{\boldsymbol{C}}^{T} \cdot \mathbf{1}$ and $\widetilde{\boldsymbol{C}}^{[PD\times J]}$ represents the complete system matrix over all possible events ($P \times D$), not just the N events measured in $\boldsymbol{x}$. The convergence of MLEM is not dependent on the initial estimate, thus the source intensities are typically initialized ($q = 0$) with a uniform distribution ($\hat{\boldsymbol{\lambda}}^{0} = \mathbf{1}$).

The number of iterations used in MLEM represents a balance between contrast recovery and image noise amplification [40]. A statistical stopping criterion can be used (e.g., a predefined tolerance on the change in the Poisson likelihood), however the likelihood monotonically increases and thus does not translate directly to an image quality metric in terms of noise or artifacts [41]. In many cases, the number of iterations is set to an arbitrary number based on past experience or, in the case presented here, reconstruction speed requirements.

The reconstruction approach described neglects *a priori* information about the source distribution, apart from the SDF constraint described below. We found that the un-regularized MLEM algorithm performed well for the source scenarios we present in this work. For more complex source distributions, techniques such as total variations regularization [42] or wavelet de-noising [43] could be explored to improve reconstruction. However, these methods currently impose challenges on real-time 3D reconstruction.

C. Scene Data Fusion

In the current implementation, the pose estimates and 3D scene model are generated at a rate of $\sim$10 Hz. The list-mode data are time-correlated with the pose estimates to provide the position and orientation of the detection system in the global image space at every event. The image space is defined with a uniformly voxelized grid based on the extent of the measurement path. The bounds of the grid are set at 5 m from the path extremes in each spatial dimension. This distance represents a balance between creating a large image space and maintaining appreciable sensitivity in every voxel. The choice of voxel size also presents a trade-off between the spatial resolution of the image space and the gamma-ray reconstruction time (which scales with the number of voxels).

The point cloud (i.e., the collection of 3D points from the SLAM-aligned laser-scans) is used to generate an occupancy grid over the voxel space, returning only the voxels that contain points and that have neighboring voxels. To reduce noise from spurious points in the cloud, we require each voxel to contain at least 10 points and have at least 4 neighbor voxels. The gamma-ray reconstruction is then constrained to the occupied voxels, limiting the source distribution to the surfaces of objects in the scene in which the LiDAR measured a reflection. The voxel constraint can improve image accuracy and decrease noise under the assumption that gamma-ray sources are not present in free-space, and the overall reduction in the number of voxels can be substantial ($> 90\%$), significantly improving reconstruction speed. A threshold is set on the number of occupied voxels (e.g., 10^5) to regulate the reconstruction time. If the threshold is crossed, the voxel size is increased.

D. GPU Acceleration

The number of poses P and voxels J used in the reconstruction will increase as the measurement progresses and the system explores new space. The memory required to store the complete system matrix (of size $P \times D \times J$) can quickly exceed the available RAM on a small onboard computer. In this case, elements of the system matrix must be computed on the fly during reconstruction. This approach can take $\mathcal{O}(\text{min})$ when performed on a low-parallelizable CPU. The use of a highly-parallelizable GPU can significantly increase computational efficiency, facilitating real-time, $\mathcal{O}(\text{s})$, imaging.

The list-mode MLEM algorithm was parallelized using the OpenCL framework [44]. OpenCL was chosen here as it can be run on CPUs, integrated graphics cards, and dedicated GPUs without any restrictions on hardware architecture (unlike e.g., CUDA [45], which is only compatible with NVIDIA products). The PRISM-v1 implementation utilizes the Intel Iris Plus Graphics 650 integrated graphics card in the onboard computer. In addition to cost, dedicated GPUs tend to be large in size and have considerable power requirements, currently prohibiting their use on small free-moving systems.

E. Visualization

Visualizing a high dimensional 3D data product including scene, pose, and gamma-ray information with enough contrast and little clutter can be challenging. In this work, we use three different methods of visualization, depending on the demonstration. First, we superimpose the gamma-ray image as iso-surfaces of intensity (i.e., a 3D contour plot) on the 3D point cloud. The point cloud is colorized by the LiDAR return intensities (i.e., a measure of reflectivity) for added contrast. Multiple viewpoints of the scene are provided to give a sense of depth. This method is used to convey the advantage of the SDF constraint over a full voxelization scheme (Sec. IV-A) because the independent 3D contours can be placed without reference to the point cloud. However, generating and transmitting 3D images can be computationally expensive and prohibit a real-time visualization framework. Therefore to demonstrate the real-time imaging performance and how the image reconstruction progresses with time (Sec. IV-B), we simply show top-down 2D projection images on a downsampled point cloud.

Following the conclusion of a measurement, high-resolution 3D images can be produced with offline processing, in $\mathcal{O}(\text{min})$. Currently the point cloud is colorized by interpolating the gamma-ray intensity map and using graphics software to render the final product. The lower 10% of the gamma-ray intensities are replaced with the LiDAR return intensities to provide higher contrast. This method is used in Sec. IV-B and IV-C. Photogrammetry software such as [46] can be used to generate colorized point clouds based on the RGB camera stream during the measurement.

IV. Results

A. SDF Constraint and GPU Acceleration

We first demonstrate free-moving 3D active coded mask imaging and the effects of the SDF constraint and GPU paral-

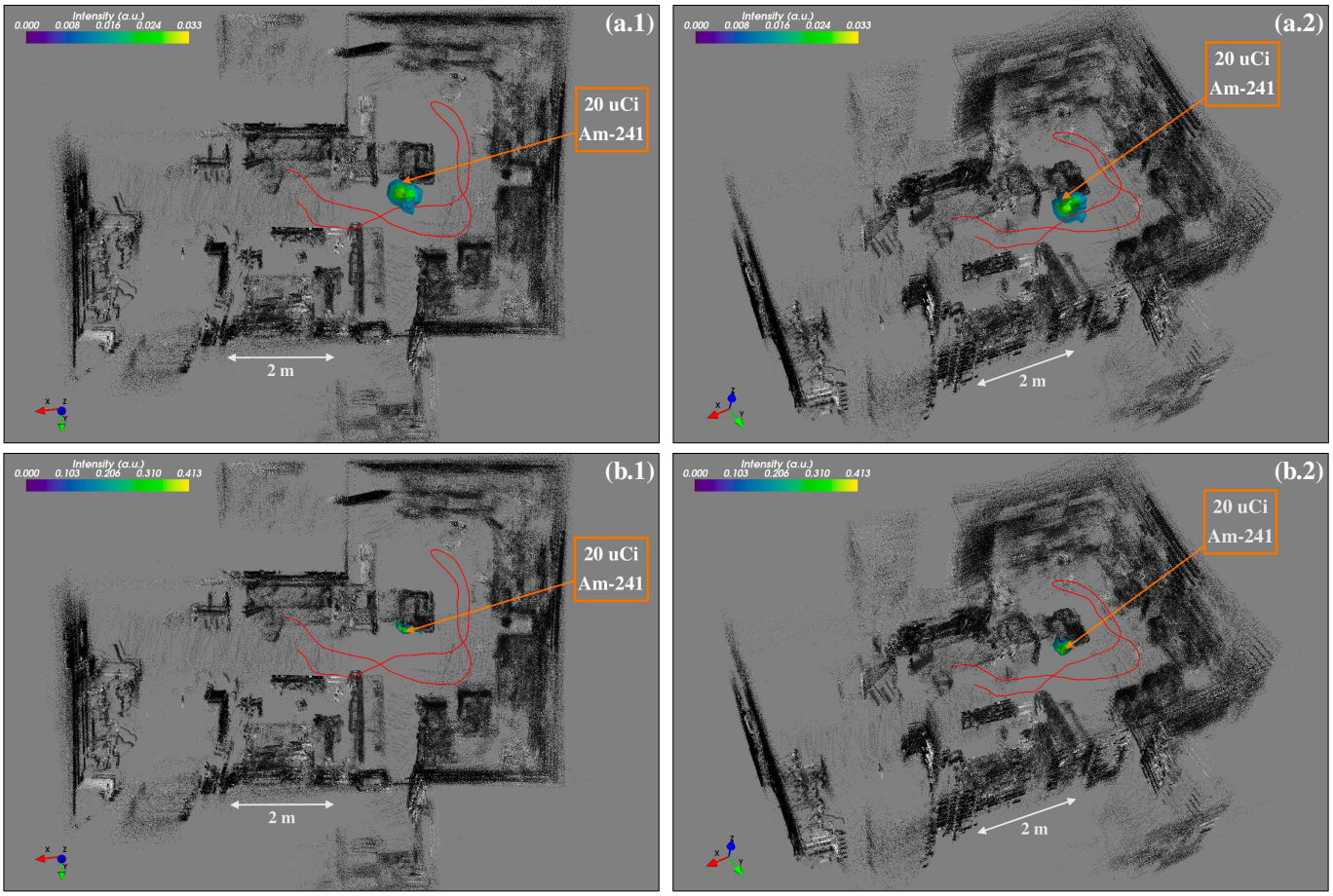

Fig. 2. (Color online) MLEM reconstruction (10 iterations) of a 35 s free-moving measurement (path shown in red) around a ^{241}Am source (marked with an arrow) in a small indoor cluttered lab space ($\sim$70 m^2). (a) Full voxelized model [(1) top-down and (2) isometric viewpoints] and (b) SDF-constrained model [(1) top-down, (2) isometric], superimposed on the 3D point cloud colorized with LiDAR return intensities. Measurement parameters: 10 cm voxel size, 2×10^6 total voxels, 5×10^4 occupied voxels (2.5% of total), 320 poses, 92 detectors, and 1095 counts in the photopeak region (59 $\pm$ 5 keV).

lelization on both image quality and computational efficiency. An unshielded point-source localization scenario in a small indoor cluttered laboratory space is considered. A 20 μCi (0.74 MBq) ^{241}Am source was placed in the corner of a large ($\sim$1 m^3) plastic case, approximately 25 cm from the top of the case. The PRISM-v1 system was walked around the lab, mapping the $\sim$70 m^2 space in less than 35 s (total of 320 poses). The 3D space surrounding the measurement path was uniformly discretized with 10 cm voxels, resulting in a total of 2×10^6 voxels and 5×10^4 occupied voxels (2.5% of the total). The list-mode gamma-ray data used in the reconstruction was limited to a 10 keV wide ROI around the ^{241}Am photopeak at 59 keV. A total of 1095 counts were collected in the ROI over the measurement from 92 detectors.

For comparison, the MLEM reconstruction was performed on both the full and SDF-constrained image space and on both the CPU and integrated GPU. Ten iterations were used to balance image quality and overall reconstruction speed. The full and constrained images are shown in Fig. 2 as 3D contour plots superimposed on a downsampled point cloud with top-down and isometric viewpoints. The color scales have units of relative intensity as the system matrix used for reconstruction is currently not quantitative. Sample run-times for the sensitivity calculation and MLEM iterations on the onboard CPU and integrated GPU are shown in Table I.

The full voxelization reconstruction results in a bias towards the measurement path and a rather diffuse estimate in space. The SDF constrained image localizes the source with a higher degree of both accuracy and precision. In addition to image quality, the SDF constraint reduces the overall dimensionality of the reconstruction, leading to significant speed increases on both hardware. The GPU-based reconstruction shows a drastic increase in reconstruction speed over the CPU ($\sim$10$\times$), improving overall run-times to $\mathcal{O}$(s).

TABLE I
SENSITIVITY AND LIST-MODE MLEM ITERATION (ITR) RUN-TIMES ON THE PRISM-V1 SINGLE-BOARD COMPUTER FOR THE IMAGES IN FIG. 2.

Hardware	Sensitivity (s)		MLEM itr (s)	
	Full	SDF	Full	SDF
Intel i7 dual-core 3.50 GHz (CPU)	550.8	14.2	49.0	1.1
Intel Iris Plus Graphics 650 (GPU)	47.3	1.3	7.5	0.2

B. Real-time Online Reconstruction

The results shown in the previous section were for data collected over the entire measurement. However, Table I shows

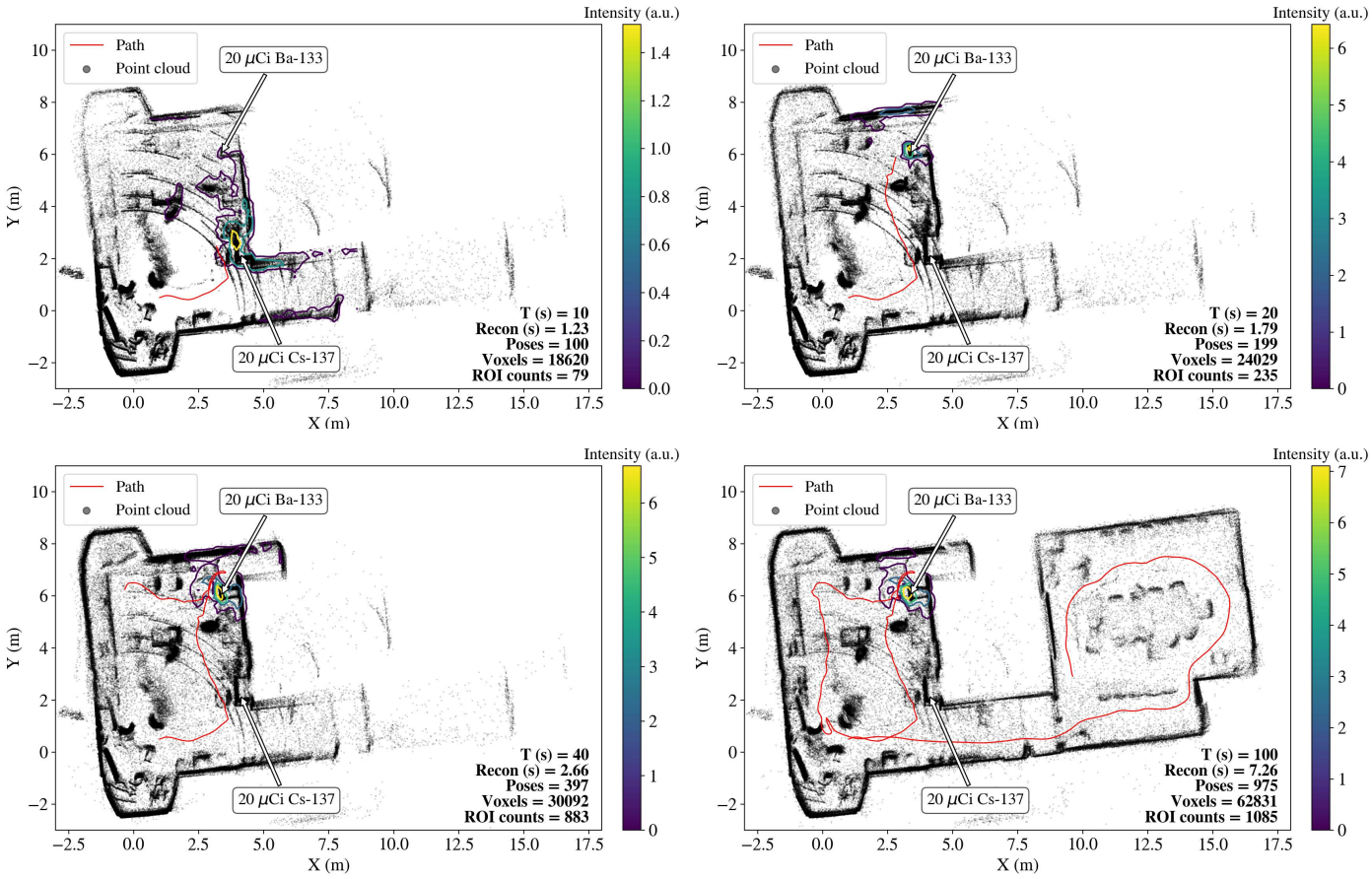

Fig. 3. (Color online) Time sequence of the top-down projection SDF-constrained MLEM reconstruction (10 iterations) during a free-moving measurement (shown with a red line) in a small indoor space (∼240 m^2). Two sources (^{133}Ba and ^{137}Cs) were placed in the scene and are marked with arrows. Reconstruction was performed on the high-energy ^{133}Ba photopeak (356 ± 5 keV). The source was correctly localized within ∼20 s.

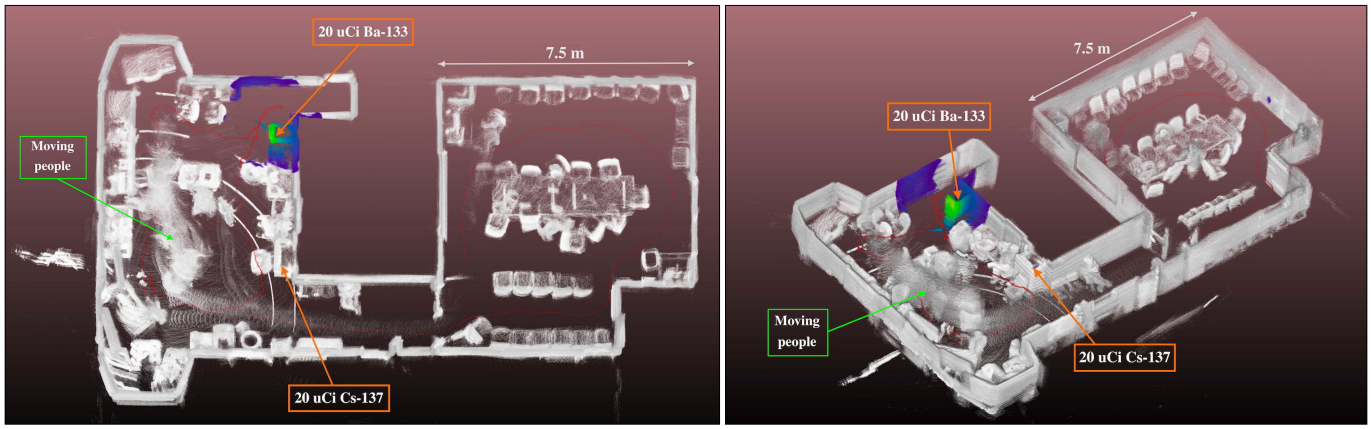

Fig. 4. (Color online) Final 3D image reconstruction from Fig. 3, shown as a colorized point cloud (visualization processed offline). The ^{133}Ba source is correctly localized to the top of the file cabinet in the back corner of the office. Point cloud tracks can be seen in the left room and are a result of people moving in the scene during the measurement. Points from the ceiling and floor have been removed for clarity.

that the SDF constrained GPU-based imaging approach can facilitate online reconstruction and return images to the user in real-time during the measurement. In this section, we demonstrate the real-time online 3D imaging capability in an indoor office space, consisting of two large rooms connected by a hallway (total area of ∼240 m^2). A 20 μCi (0.74 MBq) ^{133}Ba source and a 20 μCi (0.74 MBq) ^{137}Cs source were placed on top of filing cabinets on opposite sides of one room. The PRISM-v1 system was walked around both rooms in under 2 min. A 10 keV wide ROI was placed around 356 keV to localize the ^{133}Ba source and to demonstrate the coded mask imaging capability at higher energies. The 662 keV line from ^{137}Cs is better suited for high-energy imaging modalities (i.e., Compton imaging).

Figure 3 shows a series of top-down projection images (10 iterations MLEM) including the point cloud and pose estimates during the course of the measurement, each with a timestamp and additional reconstruction parameters such

as the number of poses, occupied voxels, counts, and the reconstruction time (sensitivity and all iterations) for the state of the measurement up to that point. The image reconstruction is always performed in 3D, and 2D projection is done only for visualization. Both the scene and the gamma-ray reconstruction update over time as new space is explored. The system first approaches the ^{137}Cs source and produces a localization estimate around its position, likely due to the Compton continuum of the 662 keV gamma-ray in the 356 keV ROI. As the system gets closer to the ^{133}Ba source, however, the image quickly corrects and localizes the ^{133}Ba source. The solution converges in < 40 s and remains roughly static as the system continues to explore new space.

Figure 4 shows multiple views of the final 3D image, visualized as a colorized point cloud (processed and rendered offline). Points from the ceiling and floor have been removed for clarity. Several blurry tracks can be seen in the point cloud, particularly in the room with the sources. The points arise from people moving through the scene during the measurement. We are currently exploring techniques such as those in [47] to remove transient points in the point cloud.

C. Wide-area Outdoor Localization

In contrast to structured light sensors based on infrared light (e.g., Kinect), the use of LiDAR facilitates SLAM in wide-area outdoor settings. To demonstrate the performance of the 3D active coded mask imaging modality in this setting, PRISM-v1 was walked toward and around a single vehicle parked among several vehicles in a large open field. A strong plutonium surrogate [194 μCi (7.2 MBq) ^{252}Cf, 530 μCi (19.6 MBq) ^{133}Ba, 35 μCi (2.0 MBq) ^{137}Cs] was placed in the open trunk. An area of $\sim$2,500 m^2 was mapped in under 1.3 min. The SDF-GPU MLEM image reconstruction (10 iterations) was run on a 10 keV ROI around the low-energy 81 keV ^{133}Ba photopeak. Figure 5 shows the results of the reconstruction as a colorized point cloud from several viewpoints. The ^{133}Ba source is correctly localized to the trunk of the car, with a hotspot accuracy on the order of tens of cm. Gamma-ray intensity is also seen on the open trunk door and the ground beneath the source and likely represents down-scattering from the primary source. In addition to 3D source localization in large outdoor settings, the results also highlight the benefit of LiDAR to produce dense, high-resolution, context-rich point clouds.

Another outdoor wide-area source search scenario measurement was performed with a collection of small and large house-like structures made of various materials (e.g., clay, brick) as well as a few steel L-shaped cargo containers. A 5 mCi (185 MBq) ^{133}Ba source was placed in one of the cargo containers and PRISM-v1 was walked around the $\sim$4,500 m^2 site in less than 2.5 min. The SDF-GPU MLEM image reconstruction (10 iterations) was run on a 10 keV ROI around the high-energy 356 keV ^{133}Ba photopeak, again to demonstrate the energy range of active coded mask imaging. Figure 6 shows the 3D reconstruction results as a colorized point cloud from several viewpoints. The gamma-ray hotspot was accurately localized to the correct cargo container among > 10 structures in the scene.

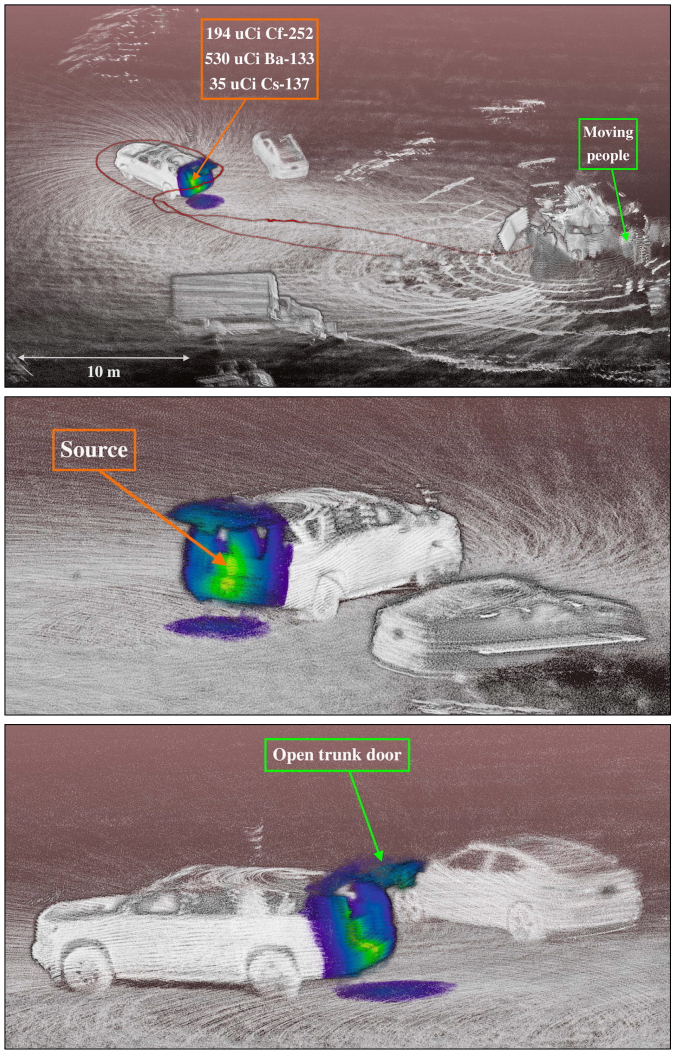

Fig. 5. (Color online) Final MLEM reconstruction (10 iterations) of ^{133}Ba from a 1.3 min measurement (path shown by the red line) around a vehicle containing a strong plutonium surrogate source in a wide-area outdoor setting ($\sim$2,500 m^2), shown as a colorized point cloud (visualization processed and rendered offline). Measurement parameters: 15 cm voxel size, 7×10^4 occupied voxels (2.9% of total), 755 poses, 91 detectors, 4542 photopeak counts (81 $\pm$ 5 keV), 10 s reconstruction time.

Since the SDF constraint currently limits the reconstruction to the point cloud (i.e., surfaces), voxels inside the containers are labelled as free and not included in the reconstruction. The source was placed inside of the container and therefore the reconstruction only shows the surface gamma-ray emission profile of the container. The dual-state occupancy model (occupied/free) could be improved with a tri-state model (occupied/free/unknown) to capture voxels inside of closed volumes or unexplored spaces (e.g., behind a wall). The reconstruction could then be performed over both occupied and unknown voxels to facilitate a full volumetric reconstruction. Open-source tools utilizing ray-casting techniques such as [48] could be used to determine tri-state occupancy.

Finally, a laser-scan mismatch can be seen in Fig 6 (the indicated structures seem to have two front walls), highlighting the fact that the gamma-ray reconstruction is currently limited by errors in the point cloud and pose uncertainties. We expect SLAM algorithms to improve with continued developments

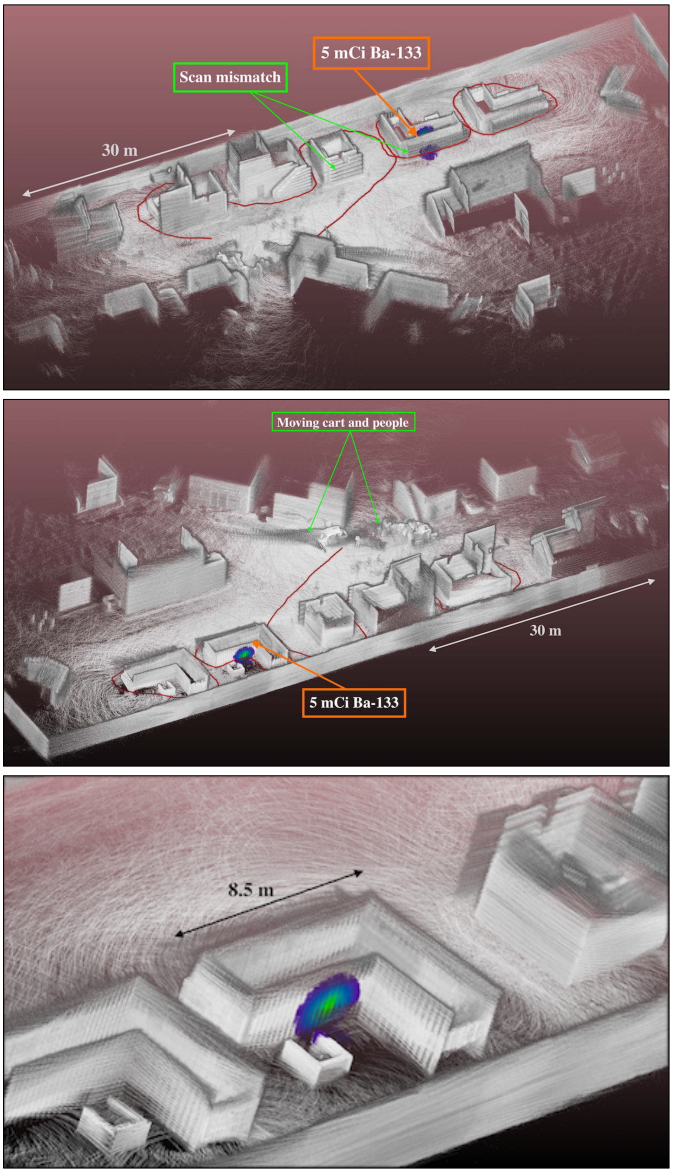

Fig. 6. (Color online) Final MLEM reconstruction (10 iterations) from a < 2.5 min measurement (path shown by the red line) in a wide-area outdoor setting ($\sim$4,500 m^2) containing several house-like structures and steel L-shaped cargo containers. A ^{133}Ba source was placed inside one of the containers and is marked with an arrow. Measurement parameters: 30 cm voxel size, 7×10^4 occupied voxels (7.3% of total), 1400 poses, 88 detectors, 9566 photopeak counts (356 ± 5 keV), 20 s reconstruction time.

in autonomous vehicles, however detailed characterizations of SLAM uncertainties will be necessary to understand their impact on free-moving gamma-ray image reconstruction and SDF.

V. Conclusions

The use of free-moving systems and the integration of contextual sensors and SDF have been shown to improve source localization and distribution mapping capabilities for applications ranging from nuclear security to consequence management. In this work, we experimentally demonstrated our approach to low-energy real-time 3D gamma-ray imaging with SDF and GPU-accelerated list-mode MLEM using a hand-held CZT-based dual-mode omnidirectional active spherical coded mask system. Source localization of unshielded point-sources was successful over energies from 59$-$356 keV, activities from 20$-$5000 μCi, and areas of size 70$-$4500 m^2. Small indoor and wide-area outdoor scenarios were considered and measurements were all < 3 min, exemplifying the capability of free-moving systems to overcome the inverse square law for efficient localization. Additional work is required to demonstrate the ability to image shielded or extended sources and map distributed sources in real-time with the active coded mask modality.

The reconstruction time increases as the image dimensionality grows during the course of a measurement. The current implementation increases the voxel size over time to limit the number of occupied voxels, but continued effort is necessary to develop a more scalable image reconstruction approach. This could include, for example, the implementation of a more robust real-time probabilistic occupancy model, the removal of transient points in the point cloud, and an adaptive non-uniform spatial discretization scheme.

References

[1] R. Arlt *et al.*, "Use of CdZnTe Detectors in Hand-Held and Portable Isotope Identifiers to Detect Illicit, Trafficking of Nuclear Material and Radioactive Sources," *in Proc. IEEE Nucl. Sci. Symp.*, 2000.

[2] J. Chin, D. K. Y. Yau, and N. S. V. Rao, "Efficient and Robust Localization of Multiple Radiation Sources in Complex Environments," *Int. Conf. Dist. Comp. Sys.*, pp. 780–789, 2011.

[3] R. T. Klann, S. C. D. la Barrera, and R. B. Vilim, "Treatment of Shielding in Real-Time Source Tracking Software," *Nucl. Tech.*, vol. 175, pp. 301–313, 2011.

[4] K. N. Shokhirev, D. Konno, T. M. Schmit, V. Ziskin, and B. R. Cosofret, "Man-portable Radiation Detector based on Advanced Source Detection, Identification, and Localization Algorithms," *in Proc. Nucl. Sci. Symp. and Medical Imaging Conf.*, 2015.

[5] F. E. Schneider and D. Wildermuth, "An Autonomous Unmanned Vehicle for CBRNE Reconnaissance," *in Proc. Int. Capathian Control Conf.*, pp. 347–352, 2011.

[6] P. Jasiobedzki, H. Ng, M. Bondy, and C. H. McDiarmid, "C2SM: A Mobile System of Detecting and 3D Mapping of Chemical, Radiological, and Nuclear Contamination," *in Proc. Sensors, and Command, Control, Comm., and Intel. Tech. for Homeland Security and Homeland Defense VIII*, vol. 7305, 2009.

[7] Y. Sanada and T. Torii, "Aerial Radiation Monitoring around the Fukushima Dai-ichi Nuclear Power Plant using an Unmanned Helicopter," *J. of Environ. Radioactivity*, vol. 139, no. 294-299, 2015.

[8] P. G. Martin, O. D. Payton, J. S. Fardoulis, D. A. Richards, and T. B. Scott, "The Use of Unmanned Aerial Systems for the Mapping of Legacy Uranium Mines," *Journal of Environment Radioactivity*, vol. 143, no. 135-140, 2015.

[9] P. G. Martin *et al.*, "3D Unmanned Aerial Vehicle Radiation Mapping for Assessing Contaminant Distribution and Mobility," *Int. J. of Appl. Earth Observation and Geoinformation*, vol. 52, pp. 12–19, 2016.

[10] R. Pavlovsky *et al.*, "3-D Radiation Mapping in Real-Time with the Localization and Mapping Platform LAMP from Unmanned Aerial Systems and Man-Portable Configurations," *arXiv:1901.05038*, 2018.

[11] C. G. Wahl *et al.*, "The Polaris-H Imaging Spectrometer," *Nucl. Instrum. Methods A*, vol. 784, pp. 377–381, 2015.

[12] PHDS Co. – Gamma Ray Imaging Detectors. [Online]. Available: http://phdsco.com/

[13] A. C. Raffo-Caiado *et al.*, "Combining Measurements with Three-Dimensional Laser Scanning System and Coded Aperture Gamma-Ray Imaging System for International Safeguards Applications," *IAEA Symp. on Int. Safeguards*, vol. 41, no. 50, 2010.

[14] L. Mihailescu, K. Vetter, and D. Chivers, "Standoff 3D Gamma-Ray Imaging," *IEEE Trans. Nucl. Sci.*, vol. 56, no. 2, pp. 479–486, 2009.

[15] H. Durrant-Whyte and T. Bailey, "Simultaneous Localization and Mapping: Part I," *IEEE Robot. Autom. Mag.*, vol. 13, no. 2, 2006.

[16] T. Bailey and H. Durrant-Whyte, "Simultaneous Localization and Mapping: Part II," *IEEE Robot. Autom. Mag.*, vol. 13, no. 3, 2006.

[17] F. Enres, J. Hess, N. Engelhard, J. Sturm, D. Cremers, and W. Burgard, "An Evaluation of the RGB-D SLAM System," *IEEE Int. Conf. on Robotics and Automation*, 2012.

[18] R. Barnowski, A. Haefner, L. Mihailescu, and K. Vetter, "Scene Data Fusion - Real-time Standoff Volumetric Gamma-ray Imaging," *Nucl. Instrum. Methods A*, vol. 800, pp. 65–69, 2015.

[19] A. Haefner, R. Barnowski, P. N. Luke, M. Amman, and K. Vetter, "Handheld Real-time Volumetric 3-D Gamma-ray Imaging," *Nucl. Instrum. Methods A*, vol. 857, pp. 42–49, 2017.

[20] D. Kim, H. Woo, Y. Ji, Y. Tamura, A. Yamashita, and H. Asama, "3D Radiation Imaging Using Mobile Robot Equipped with Radiation Detector," *in Proc. IEEE/SICE Int. Symp. on Sys. Integration*, 2017.

[21] K. Vetter, R. Barnowski, A. Haefner, T. H. Y. Joshi, R. Pavlovsky, and B. J. Quiter, "Gamma-Ray Imaging for Nuclear Security and Safety: Towards 3-D Gamma-Ray Vision," *Nucl. Instrum. Methods A*, vol. 878, pp. 159–168, 2018.

[22] A. P. Dempster, N. M. Laird, and D. B. Rubin, "Maximum Likelihood from Incomplete Data via the EM Algorithm," *J. of the Royal Statistical Society, Series B*, vol. 39, no. 1, pp. 1–38, 1977.

[23] L. Parra and H. H. Barrett, "List-Mode Likelihood: EM Algorithm and Image Quality Estimation Demonstrated on 2-D PET," *IEEE Trans. on Med. Imaging*, vol. 17, no. 2, pp. 228–235, 1998.

[24] P. N. Luke, "Single-polarity Charge Sensing in Ionization Detectors using Coplanar Electrodes," *Appl. Phys. Lett.*, vol. 65, no. 22, pp. 2884–1886, 1994.

[25] ——, "Unipolar Charge Sensing with Coplanar Electrodes - Application to Semiconductor Detectors," *IEEE Trans. Nucl. Sci.*, vol. 42, no. 4, pp. 207–213, 1995.

[26] D. Hellfeld, P. Barton, D. Gunter, L. Mihailescu, and K. Vetter, "A Spherical Active Coded Aperutre for 4π Gamma-ray Imaging," *IEEE Trans. Nucl. Sci.*, vol. 64, no. 11, pp. 2837–2842, 2017.

[27] G. D. Geronimo, G. Carini, W. S. Murray, and P. O'Connor, "Front-End ASIC for Co-Planar Grid Sensors," *IEEE Trans. Nucl. Sci.*, vol. 52, no. 5, pp. 2003–2008, 2005.

[28] M. Turqueti, R. A. Rivera, A. Prosser, J. Andersen, and J. Chramowicz, "CAPTAN: A Hardware Architecture for Integrated Data Acquisition, Control, and Analysis for Detector Development," *In Proc: IEEE Nucl. Sci. Symp.*, 2008.

[29] Intel NUC7i7BNH. [Online]. Available: https://www.intel.com/content/www/us/en/products/boards-kits/nuc/kits/nuc7i7bnh.html?wapkw=nuc7i7bnh

[30] FLIR - Flea3 1.3 MP Color USB3 Vision. [Online]. Available: https://www.ptgrey.com/flea3-13-mp-color-usb3-vision-e2v-ev76c560-camera

[31] Kowa - LM4NCL Lens. [Online]. Available: https://lenses.kowa-usa.com/ncl-series/488-lm4ncl.html

[32] Velodyne LiDAR - Puck LITE. [Online]. Available: https://velodynelidar.com/vlp-16-lite.html

[33] VectorNav Embedded Navigation Solutions - VN-200 GPS-Aided INS. [Online]. Available: https://www.vectornav.com/products/vn-200

[34] W. Hess, D. Kohler, H. Rapp, and D. Andor, "Real-Time Loop Closure in 2D LIDAR SLAM," *in Proc. IEEE Int. Conf. on Robotics and Automation*, pp. 1271–1278, 2016.

[35] E. E. Fenimore and T. M. Cannon, "Coded Aperture Imaging with Uniformly Redundant Arrays," *Applied Optics*, vol. 17, no. 3, pp. 337–347, 1978.

[36] K. Amgarou *et al.*, "A Comprehensive Experimental Characterization of the iPIX Gamma Imager," *J. of Instrum.*, vol. 11, 2016.

[37] K. P. Ziock, M. Cunningham, and L. Fabris, "Two-Sided Coded-Aperture Imaging Without a Detector Plane," *in Proc. IEEE Nuc. Sci. Symp.*, pp. 634–641, 2008.

[38] M. Galloway, A. Zoglauer, M. Amman, S. E. Boggs, and P. N. Luke, "Simulation and Detector Response for the High Efficiency Multimode Imager," *Nucl. Instrum. Methods A*, vol. 652, pp. 641–645, 2011.

[39] S. Agostinelli *et al.*, "Geant4 - A Simulation Toolkit," *Nucl. Instrum. Methods A*, vol. 506, pp. 250–303, 2003.

[40] M. Conti and M. E. Casey, "Estimating the Optimal Iteration Number in Iterative Reconstruction: A Statistical Approach," *in Proc. IEEE Nucl. Sci. Symp.*, 2007.

[41] C. Pafilis *et al.*, "A Methodology for the Estimation of the Optimal Iteration in MLEM-based Image Reconstruction in PET," *in Proc. Int. Workshop on Biomedical Eng.*, 2001.

[42] V. Y. Panin, G. L. Zeng, and G. T. Gullberg, "Total Variation Regulated EM Algorithm," *IEEE Trans. Nucl. Sci.*, vol. 46, no. 6, pp. 2202–2210, 1999.

[43] A. K. Fletcher, K. Ramchandran, and V. K. Goyal, "Wavelet Denoising by Recursive Cycle Spinning," *in Proc. Int. Conf. on Image Processing*, 2002.

[44] J. E. Stone, D. Gohara, and G. Shi, "OpenCL: A Parallel Programming Standard for Heterogeneous Computing Systems," *Computing in Sci. & Eng.*, vol. 12, no. 3, pp. 66–73, 2010.

[45] J. Nickolls, I. Buck, M. Garland, and K. Skadron, "Scalable Parallel Programming with CUDA," *ACM Queue - GPU Compting*, vol. 6, no. 2, pp. 40–53, 2008.

[46] Agisoft Metashape Standard (Version 1.5.2) (Software). (2019). [Online]. Available: http://www.agisoft.com/downloads/installer/

[47] M. Nießner, M. Zollhöfer, S. Izadi, and M. Stamminger, "Real-time 3D Reconstruction at Scale using Voxel Hashing," *ACM Trans. on Graphics*, vol. 32, no. 6, 2013.

[48] A. Hornung, K. M. Wurm, M. Bennewitz, C. Stachniss, and W. Burgard, "OctoMap: An Efficient Probabilistic 3D Mapping Framework based on Octrees," *Autonomous Robots*, vol. 34, no. 3, pp. 189–206, 2013.